A Two-dimensional Splashing Model for Investigating Impingement Characteristics of Supercooled Large Droplets

C. Wang[a,b], S. Chang[a]*, M. Leng[a], H. Wu[c], B. Yang[a]

[a] School of Aeronautic Science and Engineering, Beijing University of Aeronautics and Astronautics, Beijing 100191, China

[b] Key Laboratory for Thermal Science and Power Engineering of the Ministry of Education, Department of Thermal Engineering, Tsinghua University, Beijing 100084, China

[c] Institute of Engineering and Energy Technologies, School of Engineering and Computing, University of the West of Scotland, Paisley, Scotland PA1 2BE, United Kingdom

* Corresponding author. Email: sn_chang@buaa.edu.cn; Tel. +86(10) 8233 8008; Fax. +86(10) 8233 8008

Abstract

In this article, a two-dimensional (2D) splashing model is proposed to investigate the dynamics when Supercooled Large Droplets (SLD) impinging on a wall surface in the aircraft-icing field. Energy conservation during droplet moving and impinging is used to capture the properties of the splashed droplets. A new, statistical treatment of the droplet impinging energy and angle during the droplet-wall interaction is introduced in order to calculate the average dynamics of the SLD within a micro-control volume on wall surface. Based on the LEWICE predictions of droplet collection efficiencies and the available experimental ones, a new criterion for droplet splashing/deposition as well as a new formulation for the splashed mass is suggested. Lagrangian approach is adopted to describe the movement and impingement of droplets. The proposed model together with the previously developed droplet tracking method (DTM) for calculating droplet collection efficiency under the effect of droplet reimpingement constitute a relatively complete predicting approach of SLD impingement characteristics. Validation of the newly developed model is carried out through comparisons with available experimental droplet collection efficiencies and LEWICE predictions over several airfoil surfaces. In addition, comparisons is also made with available experimental ice shapes over a GLC-305 airfoil and a NACA23012 airfoil under both glaze condition and rime icing condition. Results show that good agreement is achieved between the current computational droplet collection efficiencies and the compared results as well as ice shapes. For further investigation of SLD impingement, properties of the droplet splashing and reimpinging during the ice accretion process are addressed.

Keywords: splashing model, SLD, collection efficiency, impingement, ice accretion

1. Introduction

Aircraft icing due to Supercooled Large Droplets (SLD) (diameter≥50μm) is a serious threat to flight safety as it is difficult to detect and can easily cause uncontrolled ice accretion beyond the deicing boots [John, 1996]. SLD, for example freezing drizzle and rain, tends to have greater inertia and is able to impinge on aircraft surfaces far beyond the limits of ice protection systems. Particularly, the impingement process is often accompanied by droplet splashing, creating a large number of splashed droplets and thus reduces the amount of water that would have been deposited by the incoming icing cloud[Roger et al., 2003]. And the splashed droplets may reimpinge on another surface, posing a great potential threat to the safety of aircraft.

Wright & Potapczuk[2004] classified the SLD dynamic effects into three orders according to the degree of influence on SLD collection, as shown in Fig. 1. The first order effect at top of the Pyramid is droplet splashing which can have a significant effect on the level of droplet collection. The second order effects including droplet deformation, droplet interaction and breakup, which have a minor effect on water collection under certain conditions. The third order effects including Basset & Saffman forces, turbulence and gravitational effects which can safely be ignored in the SLD regime. In the present work, we will focus on the droplet splashing.

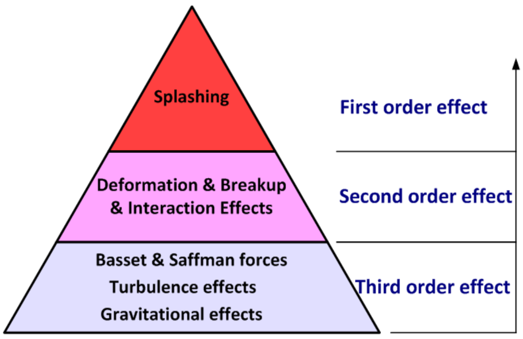

Fig. 1 Orders of SLD Dynamic Effects on SLD Icing Property

Since droplet impinging efficiency can be affected by splashing and thus change the amount of accreted ice and ice shape and therefore affects the aerodynamic performance of aircraft, further studies on this issue were expanded. Gent et al.[2003] and Potapczuk[2003] examined the relationship between the droplet size and the potential for splashing with consequent mass removal from the surface of airfoil. They found that the ice mass loss increased with the increase of the droplet size. Later on, Tan et al.[2007] and Alejandro Feo et al.[2011] used charge-coupled device (CCD) technology to record the apparent characteristics of the droplet splashing on airfoil surface. Afterward, Berthoumieu[2012] tested the droplet impingement on a rod and found that the incident droplet size, impact velocity and temperature had little effect on the splashed droplet size, but larger impact angle can result in the increase of the splashed droplet size.

On the numerical side, although current ice accretion codes can well simulate the droplet collection efficiency curves with the droplet sizes listed in Federal Air Regulation (FAR) Part 25 Appendix C, they were less successful with SLD droplet sizes due to the droplet splashing and reimpingement[Papadakis, et al. 2002; Papadakis, et al. 2004; Papadakis, et al. 2007]. Modifications of the ice accretion codes to account for mass loss due to the droplet splashing are still required. Therefore, the aim of the present work is to further develop a splashing model to improve the prediction capability of SLD impingement efficiency. It is recognized that a complete splashing model is mainly composed of determination of the critical conditions at which splashing occurs (splashing criterion), mass loss due to splashing, the splashed droplet size distribution and velocity profile. Most of the existing splashing models are in the spray field (reciprocating engines, gas turbines, spray cooling systems, inkjet printing, etc.), such as the model of Bai & Gosman[1995],Trujillo et al.[2000], Mundo et al.[1995, 2001] and Han et al.[2000]. However, because the application conditions of the models is far from SLD conditions, i.e., wall surface property, temperature, liquid water content (LWC), droplet sizes and velocities, in particular the flow structure and wall surface property, they cannot be used to predict the mass and momentum transports directly during SLD impingement. Two typical splashing models exist in SLD area are Wright splashing model[2006] and Honsek splashing model[2008]. Both of the two splashing models build on the previous spray splashing models by calibrating with the experimental data of Papadakis et al.[2007]. The modified items mainly include the splashing criteria and mass loss ratio. Detailed comparisons of the characteristics and prediction accuracy of the two splashing models are presented in Ref.[2014]. At the same time, Tan[2004] and Tan & Papadakis[2005] proposed the WSU model which was obtained by applying appropriate curve-fit equations to the predicted droplet impingement efficiency. However, this model is not widely used since it requires a high level of detail of the key parameters in the model correlations. More recently, another splashing model called SPARTE impingement model which was first designed for spray combustion application, was presented by Villedieu et al.[2012]. In this model an explicit influence of the incident angle was introduced by guessing to correct the splashing mass loss correlation. Possible future availability of a more theoretical model of the splashing mass loss may enhance the SPARTE splashing model.

The issue is that there is not yet a splashing model derived from SLD impingement directly. Although the aforementioned splashing models can result in good agreement with the experimental data in a certain range, they are directly modified or recombined from the splashing models exist in other fields, and no comment is made on how the model correlations are calibrated and derived. Therefore, it is difficult to evaluate the rationality of the models. In this paper, a new splashing model was derived based on the SLD impingement. The model was evaluated by comparing the computational droplet collection efficiencies and ice shapes with the published experimental data. This work employs the model to perform the SLD impingement calculations using Lagrangian approach in two-dimensional (2D). And the droplet tracking method (DTM) was adapted to calculate the droplet impingement efficiency under effects of droplet splashing and reimpinging[2014]. The paper is organised as follow: Firstly, droplet motion equation and droplet collection efficiency is briefly introduced. Secondly, calculations of the droplet impingement parameters, i.e. impaction energy and angle, are presented. Thirdly, detailed constructions of the model are given. Results are shown with validation against experiments and LEWICE predictions provided by Papadakis et al.[Papadakis, et al. 2002; Papadakis, et al. 2004; Papadakis, et al. 2007]. Finally, properties of the droplet splashing and reimpinging during the process of ice accretion are addressed.

2. Droplet Motion and Impingement Efficiency

In the derivation of droplet trajectory governing equation, it is assumed that: (i) the mass and heat transfer between air and droplets is ignored and the thermophysical properties of the droplets are constant; (ii) the added mass force, the Basset history force, the Magnus and Saffman forces will be neglected in the present study; (iii) droplets do not collide and coalesce.

2.1 Droplet Motion Equation

Droplet trajectory requires integration of Newton's second law and the force balance equates the particle inertia with the forces acting on the particle, given as

$$\frac{d\boldsymbol{u}_d}{dt} = K_f\left(\boldsymbol{u}_a - \boldsymbol{u}_d\right) + \frac{\left(\rho_d - \rho_a\right)}{\rho_d}\boldsymbol{g} \tag{1}$$

$$K_f = \frac{18\mu_a}{\rho_d d^2}\frac{C_d \operatorname{Re}}{24} \tag{2}$$

$$\operatorname{Re} = \frac{\rho_a\left(u_a - u_d\right)d}{\mu_a} \tag{3}$$

Here, $\boldsymbol{u}_d$ is the droplet velocity, $\boldsymbol{u}_a$ is the air velocity, t is the time, $\boldsymbol{g}$ is the acceleration due to gravity, μ_a is the molecular viscosity of the air, ρ_a is the density of the air, ρ_d is the density of the droplet and d is droplet diameter. Re is the relative Reynolds number, C_d is the drag coefficient. To account for the contribution of droplet deformation to the drag coefficient the following formulation is used[Clift et al.1978; Luxford, 2005]:

$$C_d = \left(1-\varphi\right)C_{d,sph} + \varphi C_{d,disk} \tag{4}$$

$$C_{d,sph} = 0.36 + 5.48\,\mathrm{Re}^{-0.573} + \frac{24}{\mathrm{Re}} \tag{5}$$

$$C_{d,disk} = 1.1 + \frac{64}{\pi\,\mathrm{Re}} \tag{6}$$

where $C_{d,sph}$ and $C_{d,disk}$ denote the drag coefficient of the sphere and disk, respectively, We is relative Weber number and φ is an eccentricity function of We. These parameters are given as follows:

$$\mathrm{Re} = \rho_a \left(u_d - u_a\right) d / \mu_a\,, \quad We = \rho_a \left(u_a - u_d\right)^2 d / \sigma\,,$$

$$\varphi = 1 - \left(1 + 0.007\sqrt{We}\right)^{-6} \tag{7}$$

here d is the current droplet diameter, that is, in case of droplet breakup, it denotes the secondary droplet diameter, σ is droplet surface tension coefficient. In SLD regime, as the droplet size is more than 50 μm, the terminal velocity of the droplet should be considered. Equating the total drag force F_d to the net gravity force F_g

$$F_d = F_g \Rightarrow \frac{1}{2}\rho_a u_t^2 \cdot \pi r^2 C_d = 4\pi r^3 \left(\rho_d - \rho_a\right) g / 3 \tag{8}$$

where r denotes the droplet radius and u_t denotes the terminal velocity, giving:

$$u_t = \sqrt{\frac{8rg\left(\rho_d - \rho_a\right)}{3\rho_a C_d}} \tag{9}$$

Fig. 2 shows the relationship between droplet terminal velocity, droplet velocity and air velocity. It is seen that once u_t is obtained, the initial droplet velocity can be expressed as:

$$\left.\begin{aligned} u_{dx} &= u_{ax} + u_T \sin\alpha \\ u_{dy} &= u_{ay} - u_T \cos\alpha \end{aligned}\right\} \tag{10}$$

where u_{ax} (u_{dx}) and u_{ay} (u_{dy}) denotes the local air (droplet) velocity component in the x-direction and y-direction, respectively; α denotes the angle of attack (AOA).

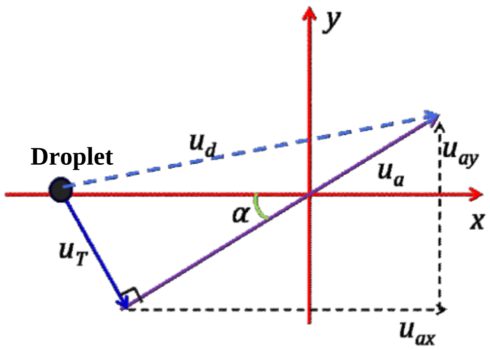

Fig. 2 Relationship between droplet terminal velocity, air velocity and droplet velocity

2.2 Droplet Impingement Efficiency

Droplet impingement efficiency which is also called droplet collection efficiency, β, is defined as the ratio of the surface mass flux of liquid droplets to the free stream mass flux of liquid droplets. Droplet collection efficiency is always below one unless the surface flux rate of droplets is equal to the free stream flux rate of droplets. In this work, the droplet tracking method (DTM) [Wang, et al., 2014] proposed in the previous study was applied to calculate the local collection efficiency influenced by droplet splashing and reimpinging.

In DTM, droplet collection efficiency of the micro-control volume *i* can be written as:

$$\beta_i = \eta_i \frac{\Delta y_i}{ds_i} \tag{11}$$

where η_i denotes the total residual ratio of the micro-control volume, Δy_i is the initial length between neighboring droplets in the free stream, and ds_i is the total separation between the trajectories on the surface. The key issue of DTM is how to determine the total residual ratio η_i.

(a) For droplet impingement without splashing, the total residual ratio is composed of two cases, initial impingement and reimpingement. For the initial impingement, all the incident mass sticks on surface, then the residual ratio is $\eta_{ns} = 1$; and for the reimpingement, the residual ratio is $\eta_{ns-re} = m_{re}/m_0$, here m_{re} and m_0 denote the splashed mass and the initial incident mass, respectively.

(b) For droplet impingement with splashing, the total residual ratio is composed of three cases, initial impingement, reimpingement and bouncing. For the initial impingement, the residual ratio is $\eta_s = 1 - f$, here f denotes the splashing mass loss ratio which is provided by splashing model; and for the reimpingement, the residual ratio is $\eta_{s-re} = m_{re}/m_0 - f$; the third case is the droplet bouncing and in this case, all the incident mass is rejected from surface, so the residual ratio is $\eta_b = 0$. Since all the cases mentioned above may occur in a micro-control volume simultaneously, the total residual ratio can be rewritten as:

$$\eta_i = \sum \eta_{ns} + \sum \eta_{ns-re} + \sum \eta_s + \sum \eta_{s-re} + \sum \eta_b \tag{12}$$

It can be seen that this method can be used to calculate the droplet impingement efficiency with and without the effects of the droplet splashing and reimpinging.

3. Calculation of SLD Impingement Parameters

Many factors can affect the droplet splashing, *i.e.*, droplet diameter (d), impact velocity (u) and angle (θ), droplet dynamic viscosity (μ_d) and density (ρ_d) and the surface tension (σ) between droplet and air. From these parameters the impaction energy parameter proposed by Mundo et al.[1995] is the most relevant:

$$K_m = \frac{(\rho_d d)^{3/4} u_n^{5/4}}{\sigma^{1/2} \mu_d^{1/4}} = \left(Oh^{-2/5} We_n\right)^{8/5} \tag{13}$$

where u_n denotes the normal component of the incident velocity, Oh is the Ohnesorge number and We_n is Weber number, given as $\mu / \sqrt{d\sigma\rho_d}$ and $\rho_d u_n^2 d / \sigma$, respectively. In addition, the conditions of wall properties, *i.e.*, roughness and liquid film, also play a major role in determining the outcome of a droplet-wall collision[Trujillo et al., 2000; Kalantari & Tropea, 2007].

3.1 Preparation

Generally, it is virtually impossible to obtain the distribution of the droplet impaction energy on airfoil by experimental method, this mainly because it is extremely difficult to measure the droplet normal incident velocity and incident angle on curved airfoil surface, especially when a large number of droplets impinge simultaneously. Therefore, the present work will employ numerical method to calculate the droplet impaction energy and angle. In addition, since the distribution of the droplet collection efficiency on airfoil surface is calculated based on the micro-control volume (grid cell lays on airfoil surface), a single droplet impaction energy and incident angle were also presented in the form of the micro-control volume. However, a micro-control volume may collect thousands of droplets as shown in Fig. 3, thus the average impaction energy $\overline{K_m}$ and the average incident angle $\bar{\theta}$ are employed to represent the impaction properties of the micro-control volume, given as:

$$\overline{K_m} = \frac{1}{n}\sum_{i=1}^{n} K_{mi} \quad \bar{\theta} = \frac{1}{n}\sum_{i=1}^{n}\theta_i \tag{14}$$

where n denotes the number of the droplets that the micro-control volume collects, θ_i denotes the angle between the droplet incident velocity vector and surface normal vector, as shown in Fig. 3. In SLD regime, when incorporating the effect of the liquid water content (LWC) and droplet density, the impaction energy parameter can be written as[Wright, 2006]:

$$\overline{K_y} = \left(LWC/\rho_d\right)^{-3/8}\sqrt{\overline{K_m}} \tag{15}$$

Here LWC and ρ_d are input parameters during the calculation of SLD impingement.

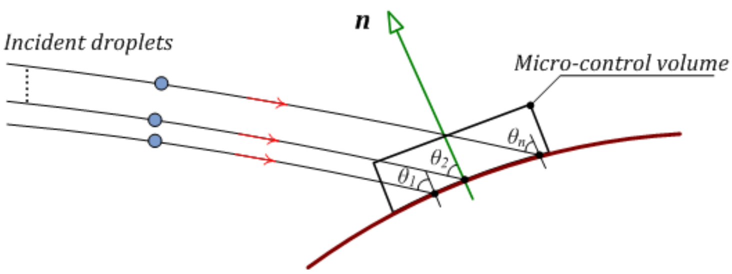

Fig. 3 Droplet collection of the micro-control volume on airfoil surface

Another parameter that represents the impaction property of the micro-control volume is the splashing mass loss ratio f. It is a ratio of the splashed droplet mass to the incident droplet mass. In the present work, f was calculated by the following expression:

$$f = \frac{\beta_L - \beta_e}{\beta_L} \tag{16}$$

where β_e denotes the experimental droplet collection efficiency, β_L denotes LEWICE's value. Both values were obtained by surveying the data in Refs.[Papadakis, et al. 2002; Papadakis, et al. 2004; Papadakis, et al. 2007]. However, $\overline{K_m}$ and $\bar{\theta}$ are not available in the literature. Therefore, calculations of $\overline{K_m}$ and $\bar{\theta}$ were expanded in order to explore the effects of $\overline{K_m}$ and $\bar{\theta}$ on f in the current study. Prior to conducting the aimed computations, it is necessary to validate the computational method.

3.2 Method Validation

As droplet collection efficiency is the result of the interaction between the airflow and the discrete droplet phase, thus the distribution of the droplet collection efficiency on the impingement surface, to a large extent, reflect the accuracy of the CFD methodology. Therefore, to assess the accuracy of present CFD methodology, computations of the droplet collection efficiencies were compared to the ones obtained by LEWICE code[Papadakis, et al. 2002; Papadakis, et al. 2004; Papadakis, et al. 2007] in SLD regime. It is believed that if the agreement between the current predictions and the LEWICE results is physically acceptable, then the present calculations of $\overline{K_m}$ and $\bar{\theta}$ can be used to represent the impinging properties obtained by LEWICE in the references.

For the purpose of comparison, six test conditions were selected for the numerical simulations. The airfoil models applied in the calculation are MS-317[Papadakis, et al. 2002; Papadakis, et al. 2007] and NACA23012[Papadakis, et al. 2004] and both models have a chord of 0.914 m. The angle of attack (AOA) is 0° for MS-317 and 2.5° for NACA23012. MVD of the droplets are 79, 94, 111, 137, 168 and 236 μm, respectively. And the corresponding LWCs are 0.496, 0.22, 0.73, 0.68, 0.75 and 1.89 g/m^3, respectively. The flow velocity is 78.25 m/s.

The airflow governing equations (omitted for the sake of conciseness) and the droplet motion equation were solved using ANSYS Fluent 14.0. Turbulent predictions for the continuous phases were obtained using the S-A model and the solution gradients at the cell centers were evaluated by Green-Gauss method. The pressure-velocity coupling equation was taken care of with the phase-coupled Semi-Implicit Method for Pressure Linked Equations (SIMPLE) algorithm. Grid independence checking was expanded by comparing the solutions of a typical test case obtained by utilizing different grid sizes. It was found that 107000-grid is economic with sufficient grid independence for all subsequent simulations in the present study.

Fig. 4(a)~(d) and Fig. 5(a)~(b) show the comparisons between the current computational droplet impingement curves and LEWICE results. Good agreement are observed between the present predictions and LEWICE results especially for MVD=137 μm and MVD=111 μm, as shown in Fig. 4(c) and Fig. 5(a). A slight separation is noted close to the impingement limits at MVD=79, 94, 168 and 236, as shown in Fig. 4(a)~(b), Fig. 4(d) and Fig. 5(b). In order to assess the agreement between the two sets of data quantitively, the standard variance

$D_s(\beta_i)$ was introduced. During this program, the current results was taken as inspection objects while the LEWICE data was deemed as a mathematical expectation. The standard variance can be obtained by the following expression:

$$D_s(\beta_i)=\left[\frac{1}{n}\sum_{i=1}^{n}\left[\beta_i-\beta_{L(i)}\right]^2\right]^{1/2} \tag{17}$$

where n denotes the number of discrete data and in the present work, data was taken every 10mm. We have:

Table 1 Standard variance at different MVDs

MVD/μm	79	94	111	137	168	236
$Ds\,(\beta_i)\times10^2$	1.33	1.34	1.09	1.07	1.34	1.18

Obviously, $D_s(\beta_i)$ represents the average degree of the deviation of the present results from the LEWICE data. A smaller $D_s(\beta_i)$ means better agreement between the two sets of results. It is clearly seen from Table 1 that the standard variance at different MVDs is very low and this indicates that the accuracy of the present methodology are physically acceptable. It should be noted that both present results and LEWICE data are not coupled SLD splashing effects.

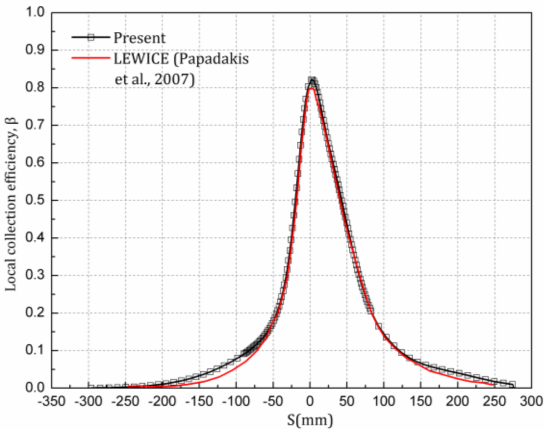

（a）MVD=79μm

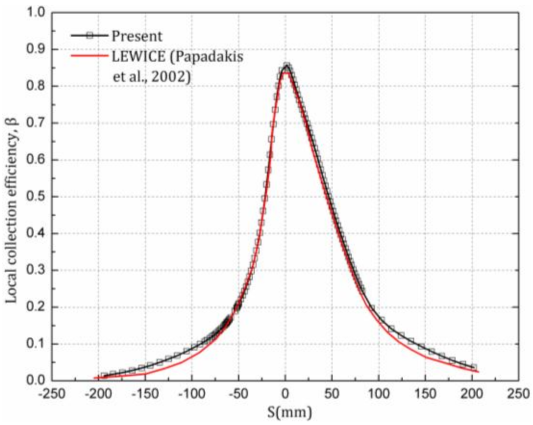

（b）MVD=94μm

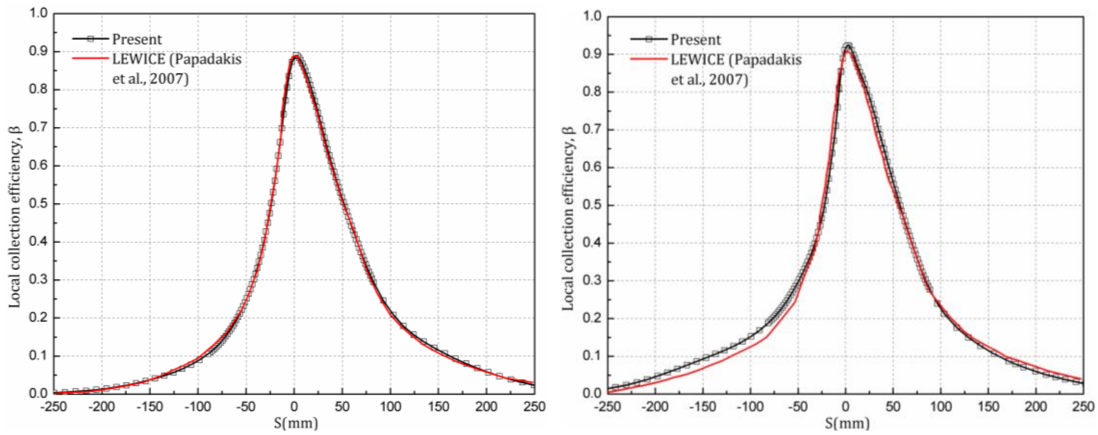

（c）MVD=137μm （d）MVD=168μm

Fig. 4 Comparison of the present droplet collection efficiency with LEWICE results for MS-317 Airfoil at MVD=79μm, 94μm, 137μm and 168μm (“-” lower side, “+”upper side)

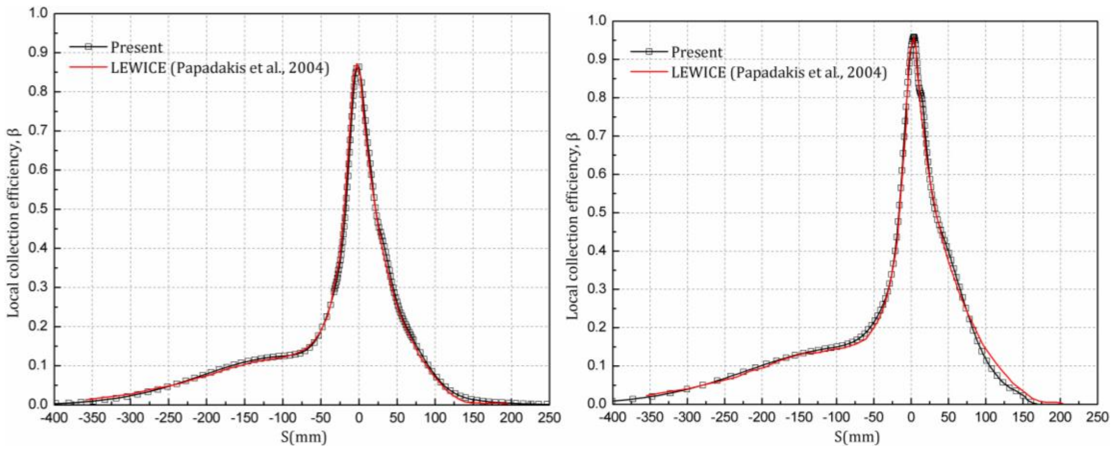

（a）MVD=111μm （b）MVD=236μm

Fig. 5 Comparison of the present droplet collection efficiency with LEWICE results for NACA23012 Airfoil at MVD=111μm and MVD=236μm (“-” lower side, “+”upper side)

3.3 Droplet Impaction Energy, Incident Angle

Distributions of the droplet impaction energy $\overline{K_m}$ and incident angle $\bar{\theta}$ are shown in Fig. 6(a)~(b) and Fig. 7(a)~(b). Note that droplet incident angle $\bar{\theta}$ is expressed in the form of cosine function $cos\bar{\theta}$. It is seen that the maximum value of $\overline{K_m}$ is located at the stagnation point (S=0). And the larger of the droplet size, the greater of the impaction energy when subjected to similar external condition. Similar to $\overline{K_m}$, the distribution of $cos\bar{\theta}$ also performs a decreasing tendency from the stagnation point to the impingement limit. Now the droplet impaction energy and the incident angle are available in the region of the droplet impingement, so the splashed mass loss f described by Eq.(17) can be determined at given $\overline{K_m}$ and $cos\bar{\theta}$. The results of ($cos\bar{\theta}$, $\overline{K_m}$, $\overline{K_y}$, f) were listed in Appendix Table 1 and Table 2.

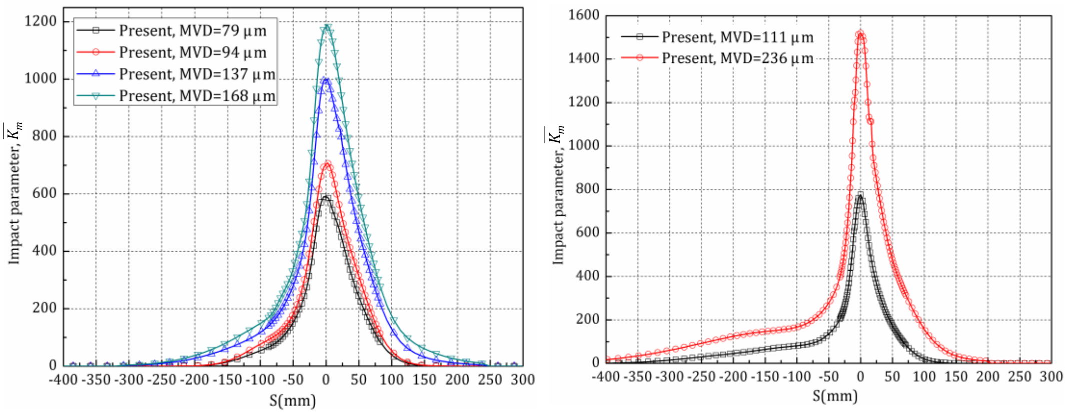

（a） MS-317 （b） NACA23012

Fig.6 Distributions of $\overline{K_m}$ on airfoil surfaces

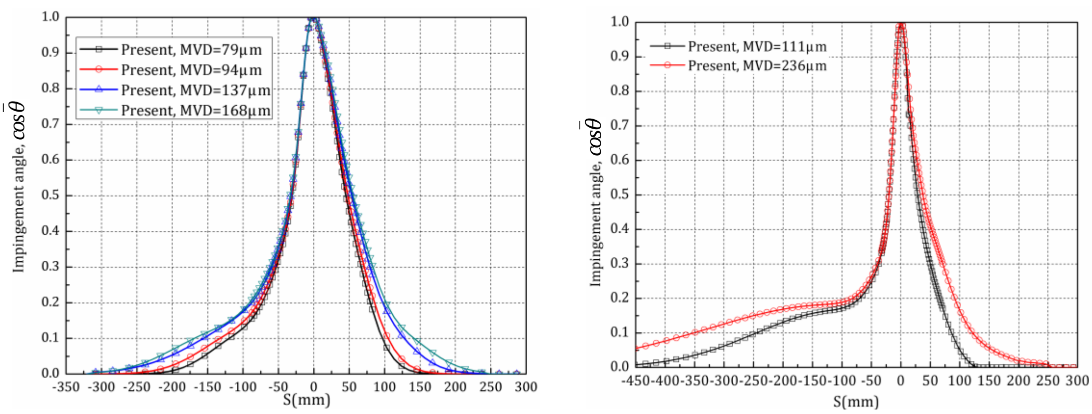

（a） MS-317 （b） NACA23012

Fig.7 Distributions of $cos\bar{\theta}$ on airfoil surfaces

4. The Proposed SLD Splashing Model

Based on the droplet impingement data prepared in the aforementioned section, a splashing model composed of the splashing criteria, splashing mass loss ratio, splashed droplet properties will be proposed in this section. As the splashing model is for single incident droplet, therefore, $\overline{K_y}$ and $\bar{\theta}$ are instead by K_y and θ in the following section.

4.1 Splashing Criteria

The mass loss ratio f in the appendix has been expressed as the function of $K_y/cos\theta$, as shown in Fig. 8. Power function was used to fit the discrete data points. The best fitting equation was given as:

$$f_{cr} = 9.686\times10^{-2}\left(\frac{K_y}{cos\theta}\right)^{0.4853} - 0.9798 \tag{18}$$

In this work, it is assumed that splashing must occur if $f_{cr} > 0$, and this is always the case in the published literature [Trujillo et al., 2000; Cossali et al., 1997]. Then we have:

$$\frac{K_y}{cos\theta} > 117.7 \tag{19}$$

Eq. (19) is the splashing criteria of the present splashing model.

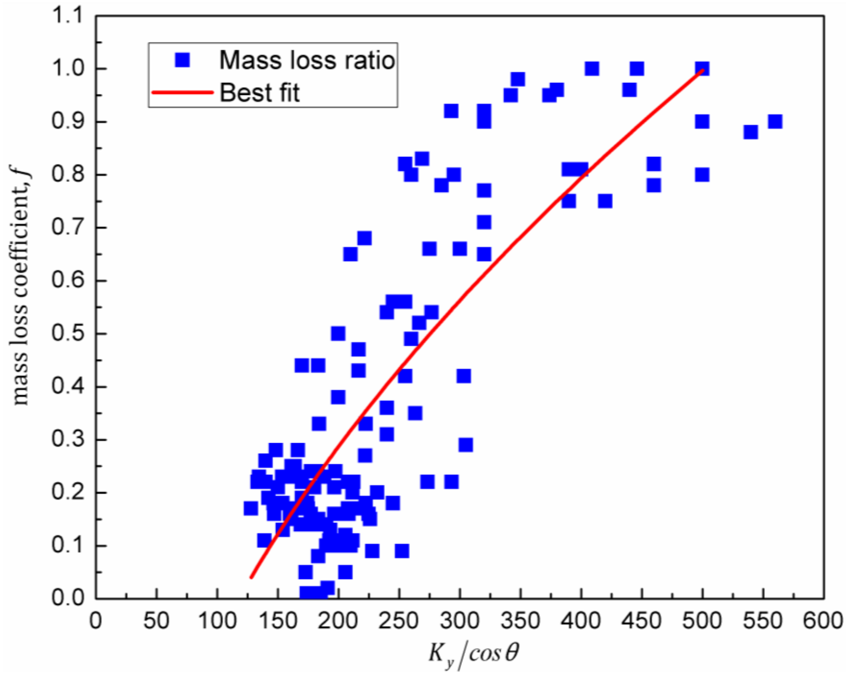

Fig. 8 Distribution of the splashing mass loss ratio under the effect of droplet impaction energy and incident angle

4.2 Splashing Mass Loss Ratio

The splashing mass loss ratio f in Appendix Table 1 was plotted as a function of the impaction energy K_y and the incident angle function $cos\theta$ as shown in Fig. 9 and Fig. 10. As can be seen that the SLD splashing mass loss data performs a gradually decreasing tendency with the increase of K_y and $cos\theta$. Comparing with Fig. 6 and Fig. 7, it is interesting to note that the splashing mass loss ratio is lower at the stagnation point but higher close to the impingement limit. The correlations that fit the data are given as:

$$f_{K_y} = 1.14EXP\left\{-\left[\left(K_y + 44.31\right)/110.2\right]^2\right\} \tag{20}$$

$$f_{cos\theta} = 0.85EXP\left(-2.785\,cos\theta\right) \tag{21}$$

In order to incorporate both effects of the droplet impaction energy and incident angle on the splashing mass loss, the following correlations are proposed:

$$f = \lambda \cdot f_{K_y} + (1-\lambda) \cdot f_{\cos\theta} \quad (0 < \lambda < 1, \ \ 0 \le f \le 1) \tag{22}$$

where λ is an interpolation coefficients. After several tests, it was found that the predictions of the splashing mass loss ratio obtained at $\lambda = 0.2$ show better agreement as depicted in Fig. 9 and Fig. 10.

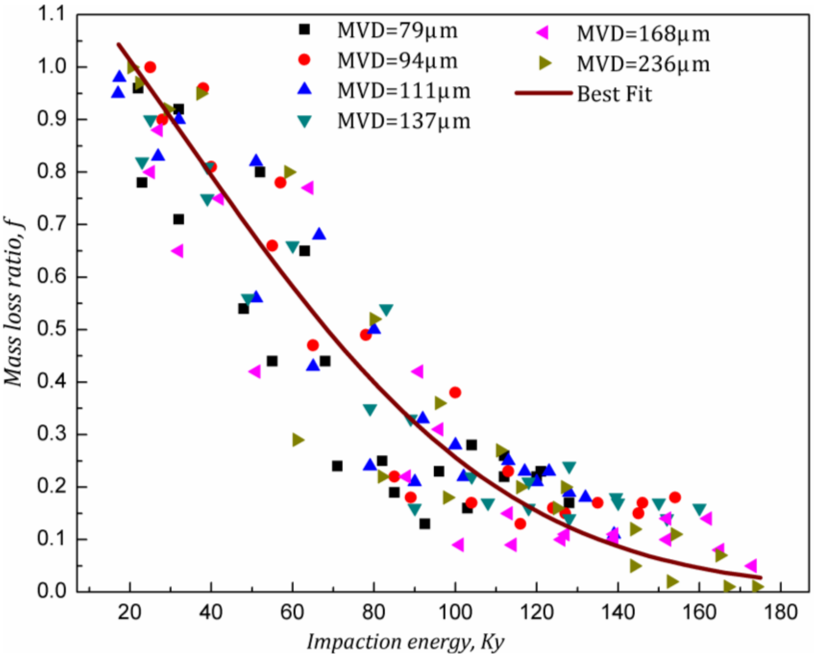

Fig.9 Effect of droplet impaction energy on splashing mass loss

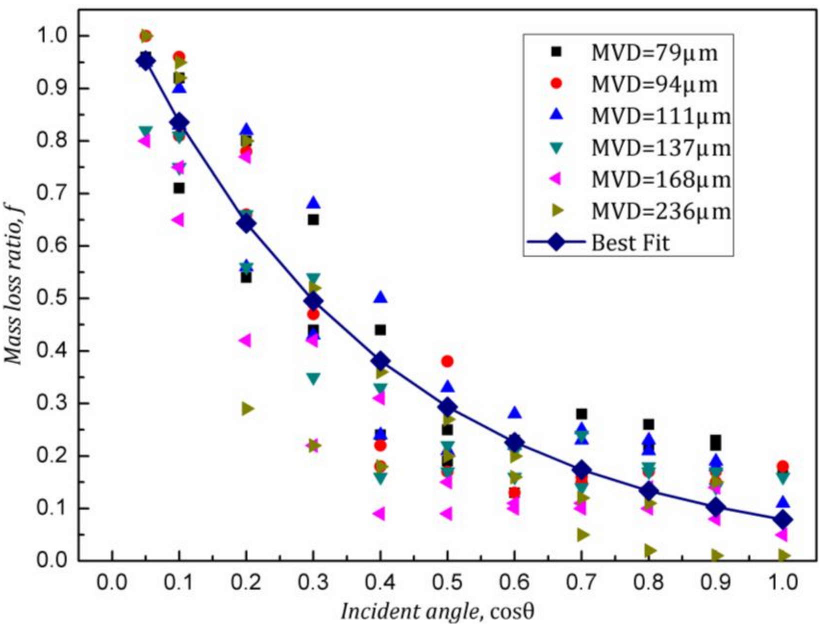

Fig.10 Effect of incident angle on splashing mass loss

4.3 Splashed Droplets

The splashed droplets' velocities can be obtained by solving the equation of energy conservation. The principle of the energy conservation of the droplet deposition and splashing has been applied in Refs.[Bai et al.,1995; Mundo et al., 1995] for model development and validation. The energy conservation equation is:

$$E_{K,i} + E_{\sigma,i} = E_{K,s} + E_{\sigma,s} + E_c \tag{23}$$

where $E_{K,i}$, $E_{K,s}$ denote the kinetic energy of incident droplet $m_i u_i^2/2$ and the kinetic energy of splashed droplet $m_s u_s^2/2$, respectively. $E_{\sigma,i}$, $E_{\sigma,s}$ denote the surface tension energy of incident droplet and splashed droplet, given as $\pi\sigma d_i^2$ and $\pi\sigma \mathrm{N} d_s^2$ (N denotes the amount of the splashed droplets), respectively. E_c is the critical kinetic energy below which no splashing occurs:

$$E_c = \frac{1}{2} m_i \left(u_{i,nk}^2 + u_{i,tk}^2 \right) \tag{24}$$

where $u_{i,nk}$, $u_{i,tk}$ denote the normal and tangential components of incident velocity at the critical splashing condition, respectively. For $u_{i,nk}$, it can be obtained by solving Eq. (19), given as:

$$u_{i,nk} = 1968\left(\sigma^2 \mu_d\right)^{1/5} \left[\frac{(cos\,\theta)^{8/3}\, LWC}{\rho_d^2 d} \right]^{3/5} \tag{25}$$

$u_{i,tk}$ is then calculated by:

$$u_{i,tk} = u_{i,nk} \tan\theta \tag{26}$$

To solve Eq. (23) one needs to know the properties of the splashed droplets, *e.g.* the quantity of the splashed droplet N, size d_s or velocity u_s. When splashing occurs, the splashed droplets generally have different sizes and velocities, as shown in Fig. 11(a). Furthermore, they are very sensitive to the wall surface and liquid properties as described in Refs.[Trujillo et al., 2000; Cossali et al., 1997]. It is a great challenge to track every produced droplet in numerical simulation, particularly for the SLD issue in which a large amount of droplets impact. For the current 2D simulation, however, it is assumed that for a single incident droplet, the total splashed droplets were taken as an equivalent droplet, as demonstrated in Fig. 11(b). Then the characteristic diameter of the equivalent droplet d_s is given by:

$$d_s = \sqrt[3]{f}\, d \tag{27}$$

Therefore, the surface tension energy of the splashed droplet $E_{\sigma,s}$ is finally rewritten as:

$$E_{\sigma,s} = \pi \sigma d^2 f^{2/3} \tag{28}$$

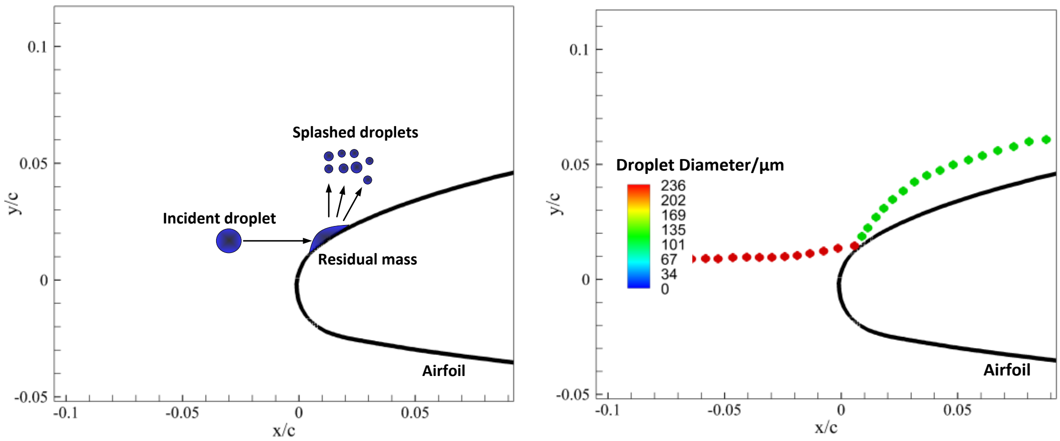

(a) A real splashing case (b) Simplification of droplet splashing

Fig. 11 Simplification of droplet splashing for 2D simulation

Now, the splashed velocity magnitude u_s can be obtained from Eq. (23), given as:

$$u_s = \left\{ \left[u_i^2 - u_{i,nk}^2 \left(1 + \tan^2\theta\right) + 12\sigma\left(1 - f^{2/3}\right) / \left(\rho_d d_i\right) \right] / f \right\}^{1/2} \tag{29}$$

The direction of the splashed velocity can be determined from the reflect angle θ_r. Mundo et al.[1995] performed droplet impact tests on two stainless steel surfaces, rough surface and smooth surface. In their report, the reflection angle of the splashed droplets was expressed as a function of the impingement angle of the primary droplet, as shown in Fig.12. For the present work, as the impinging surface roughness is unavailable, a conservative correlation is proposed that reduces the effect of surface property:

$$\theta_r = -9.11 \times 10^{-2} \theta^{-1.172} + 1.276 \tag{30}$$

Then in Cartesian coordinate system, the components of u_s were given as:

$$u_{s,x} = u_s \cos\theta_r \tag{31a}$$

$$u_{s,y} = u_s \sin\theta_r \tag{31b}$$

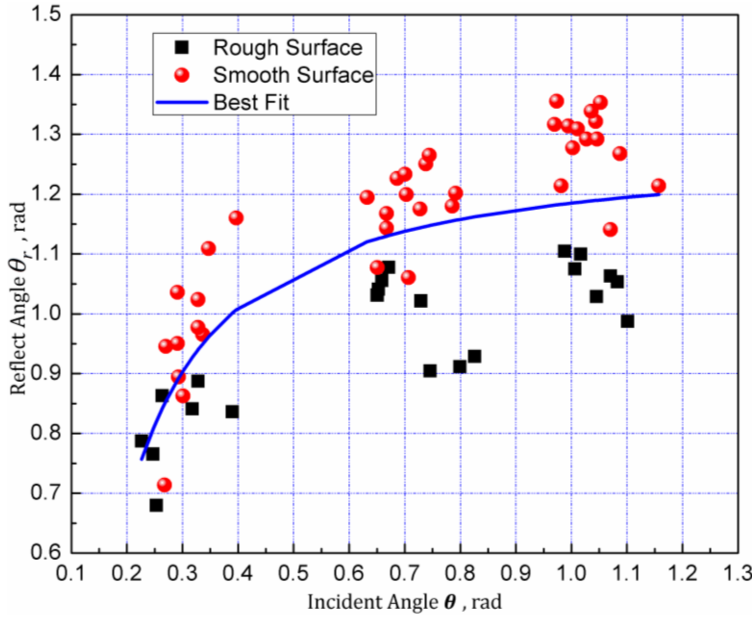

Fig. 12 Curve fitting of dependency of the reflection angle θ_r on the impingement angle θ for the smooth and the rough surface

Here, a complete two dimentional splashing model has been presented. The splashing model can be incorporated into Fluent by user defined function (UDF). The macros used are mainly DEFINE_DPM_DRAG and DEFINE_DPM_BC.

5. Results and Discussion

In this section, the performance of the present splashing model was evaluated by comparing the predictions of the droplet impingement characteristics with available experimental data and published computational results using LEWICE code[Papadakis, et al. 2002; Papadakis, et al. 2004; Papadakis, et al. 2007]. Two typical SLD icing conditions were applied to assess SLD splashing on ice accretion and to demonstrate droplet splashing and reimpinging behaviors during ice accretion.

5.1 Validation: Droplet Collection Efficiency

A typical case of the droplet splashing on the leading edge of an airfoil obtained by the current splashing model is shown in Fig. 13. As droplet impaction energy and incident angle are varying at different impingement points, the rejected droplet sizes are also different. Additionally, it is interesting to note that the trajectories of the splashed droplets perform a parabolic shape around the airfoil and moving back towards the airfoil rear. The point is that the sizes of the splashed droplets have been reduced greatly compared to the original incident ones, so they can be easily carried by the airflow and may impinge on other parts behind the airfoil leading edge causing unexpected ice accretion in icing conditions.

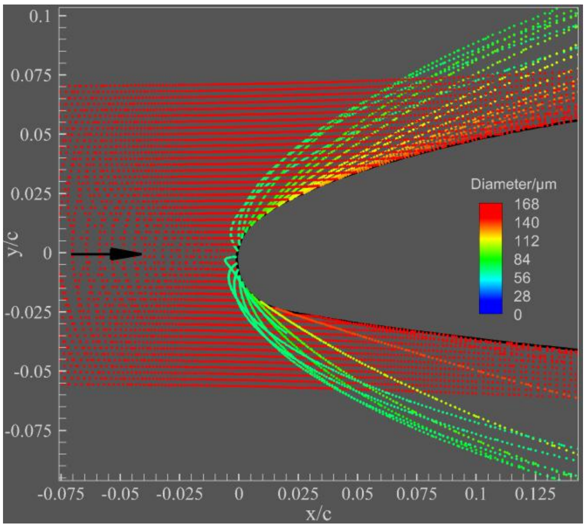

Fig. 13 Droplets impingement and splashing on airfoil surface (Droplets moving from left to right)

Comparisons of the droplet collection efficiency curves between the numerical results and experimental data were presented in Fig.14. The computational conditions are the same with the above-mentioned in section 3.2. It can be seen that the levels of the droplet collection efficiency throughout the impinging range and the impingement limits obtained by the current splashing model show much better agreement with the experimental observations compared to LEWICE ones, especially for MVD=168, 111 and 236 μm, as shown in Fig.14 (d), Fig.14 (e) and Fig.14 (f), respectively. For MVD=79 μm (Fig.14 (a)), 94 μm (Fig.14 (b)) and 137 μm (Fig.14 (c)), however, slight dismatches were observed around the stagnation point (S=0) and the current predictions are bout 10% higher than the experimental data. The main reason for the dismatch could be attributed to the fitting method introduced in section 4.2. And in the fitting method, the data satisfying the fitting equation was used instead of the discrete real mass loss ratio as shown in Fig.9 and Fig.10. The comparisons show that the current splashing model helped to bridge the gap between the predicted droplet collection efficiencies and experimental observations, particularly in the area close to the impingement limits.

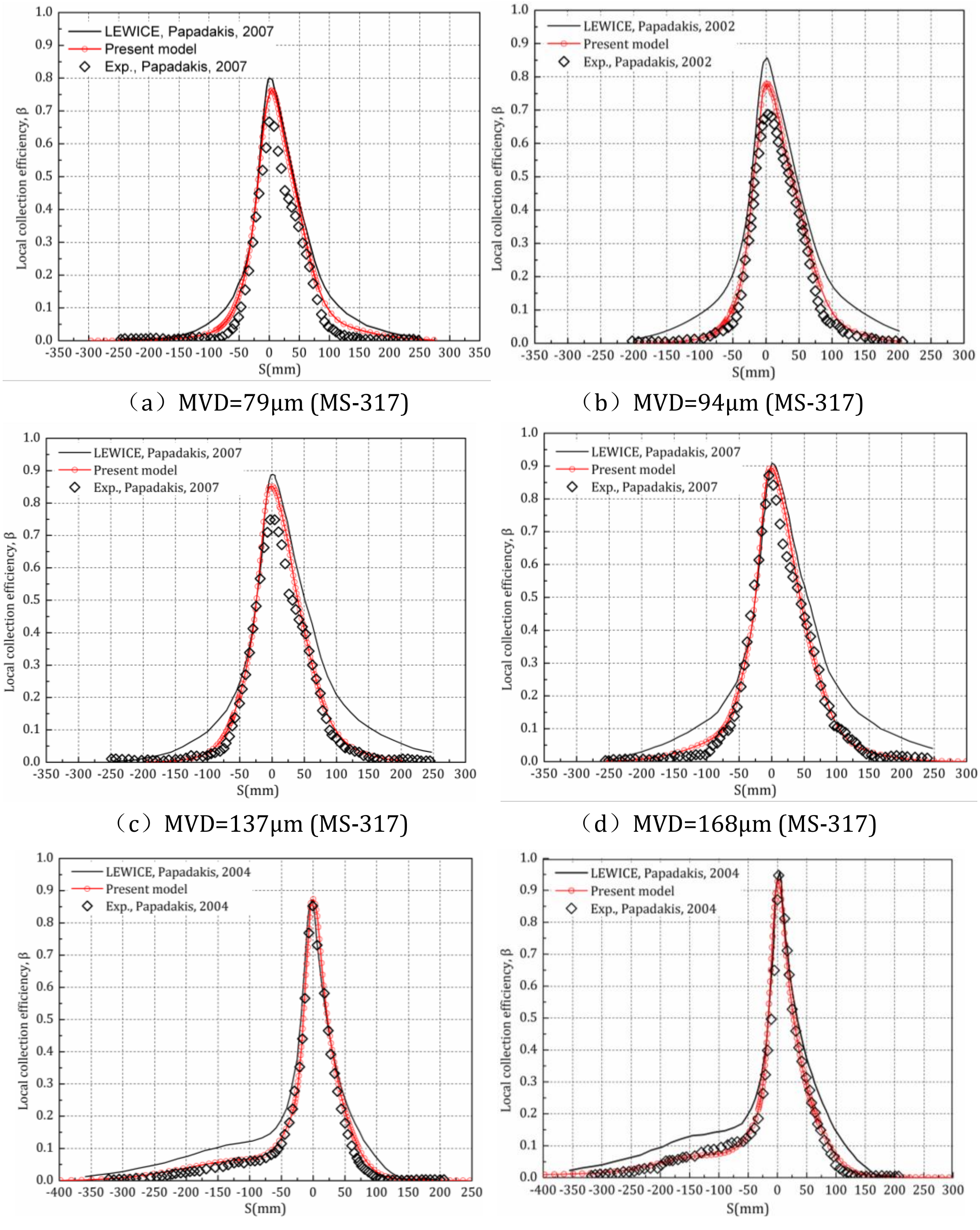

（a）MVD=79μm (MS-317) （b）MVD=94μm (MS-317)

（c）MVD=137μm (MS-317) （d）MVD=168μm (MS-317)

(e) MVD=111μm (NACA23012) (f) MVD=236μm (NACA23012)

Fig. 14 Comparison of impingement efficiency distribution on the surfaces of MS-317 and NACA 23012 airfoils at AOA=0°

For further evaluation of the splashing model, extended comparisons of droplet impingement on other airfoils, *i.e.* GLC305 and NACA-$65_2$415, were expanded, as shown in Fig.15(a)~(b). As expected, good matches are also observed between the current predictions and the experimental data throughout the impinging range. Similarly, a slight discrepancy between the present results and the experimental data was observed near the stagnation point at MVD=79 μm for the two airfoils, as shown in Fig.15(a) and Fig.15(b). And the predictions are about 10% over the experimental data.

The above comparisons were performed at AOA=0 °, as a comparison, Fig.16 presents the droplet impingement on the airfoil of NACA-$65_2$415 at AOA=4 °. Good agreement is also observed between the present predictions and the experimental results except a little discrepancy in the area of surface distance from 25 mm to 100 mm on the lower surface. The reason could be that the present 2D splashing model assumes one secondary droplet reflected from surface whereas in the real process there are many secondary droplets with different sizes and velocities, which depends on a large number of factors as mentioned in section 3. Despite this, it is seen that the agreement between the present calculations and the experimental results is satisfactory.

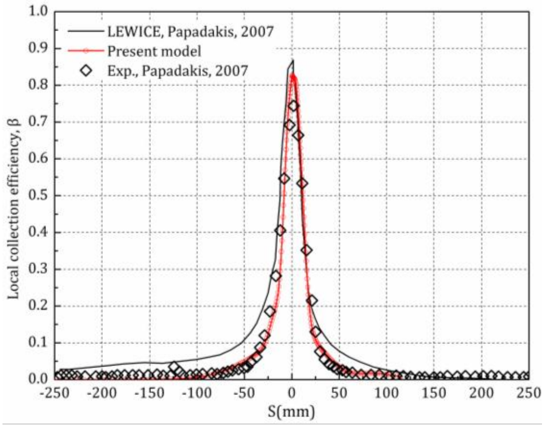

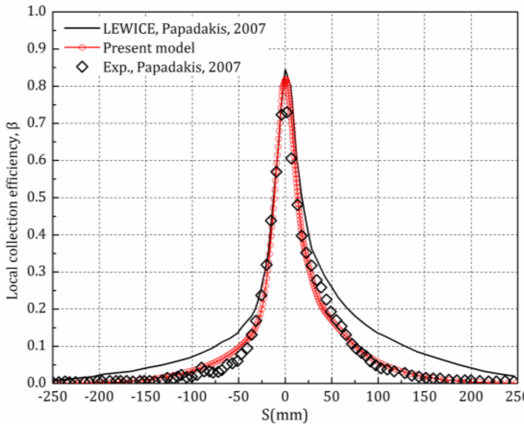

(a) MVD=79μm (GLC305) (b) MVD=79μm (NACA-$65_2$415)

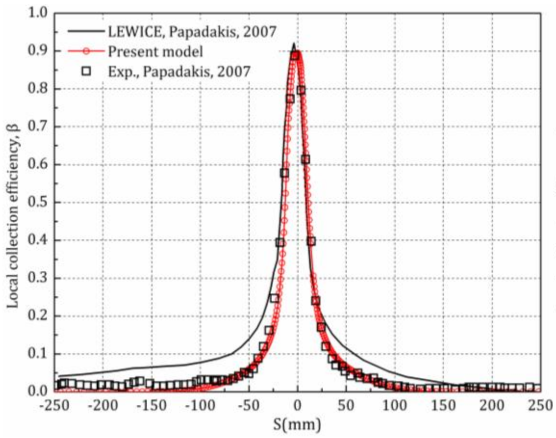

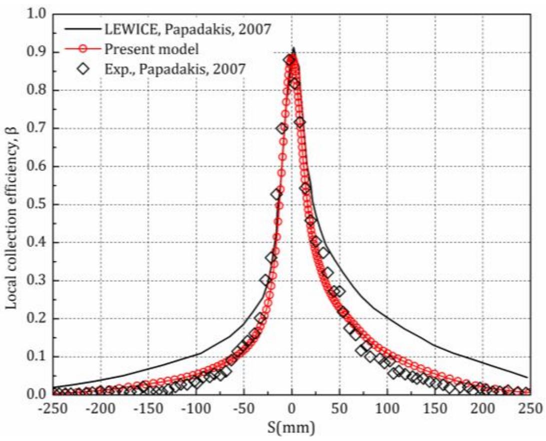

(c) MVD=137μm (GLC305) (d) MVD=137μm (NACA-$65_2$415)

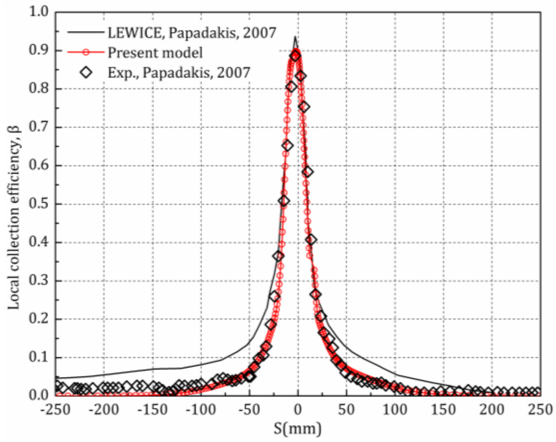

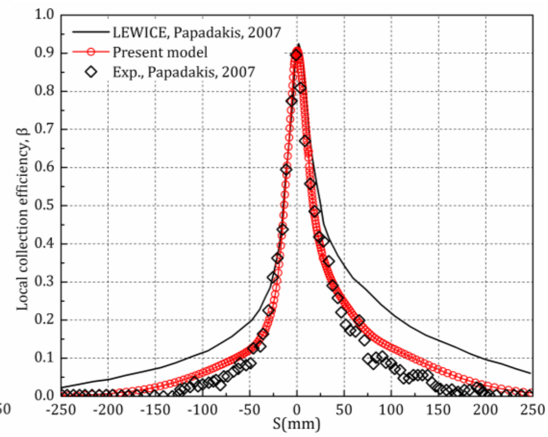

(c) MVD=168μm (GLC305) (d) MVD=168μm (NACA-$65_2$415)

Fig.15 Comparison of impingement efficiency distribution on the surfaces of GLC305 and NACA-$65_2$415 airfoils at AOA=0°

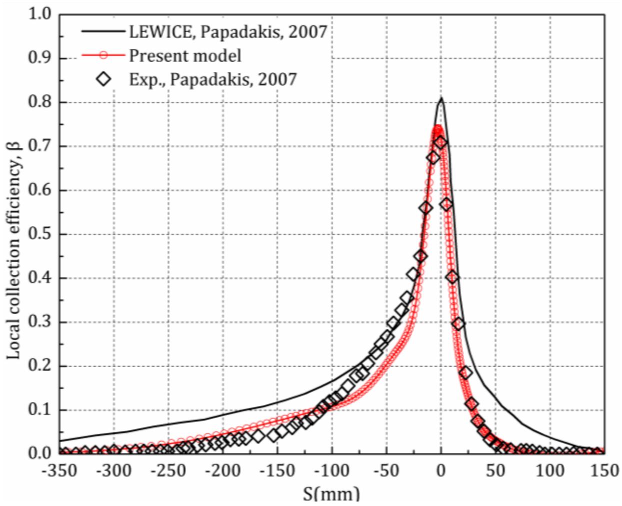

(a) MVD=79μm

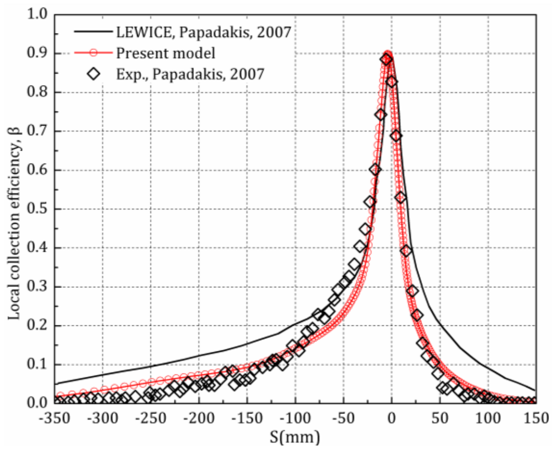

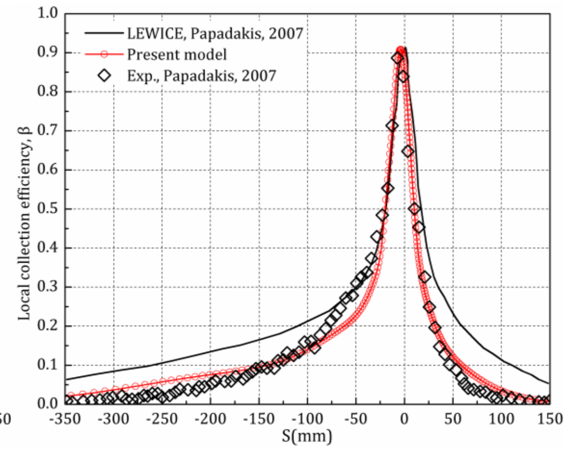

(b) MVD=137μm (c) MVD=168μm

Fig.16 Comparison of impingement efficiency distribution on the surfaces of NACA-652415 airfoils at AOA=4°

5.2 Validation: Ice Shape

For the purpose of comparison, two airfoil models and two typical icing conditions, GLC305 airfoil in glaze icing condition[Judith, 2007] and NACA23012 airfoil in rime icing condition[Wright et al., 2008], were selected for the numerical simulations, as summarized in Table 2. Fig.17 (a) and (b) show the leading part of standard models of GLC305 and NACA23012 clean airfoil and the "iced" meshes, respectively. Time interval for ice shape update and mesh generation was two minutes. As the current work focuses on droplet impingement characteristics, thus descriptions on mass & heat equations solving were omitted for briefness. For details of the strategies of ice accretion simulation, one was suggested to refer [Li et al., 2011].

Table 2 Geometric and flow conditions for ice accretion simulation

Items	Chord (m)	*t* (°C)	Ma	LWC (g/m³)	MVD (μm)	AOA (°)	Time (min)
GLC305	0.914	-10	0.32	0.7	119	2	10
NACA23012	1.828	-23.3	0.32	0.55	225	2	10

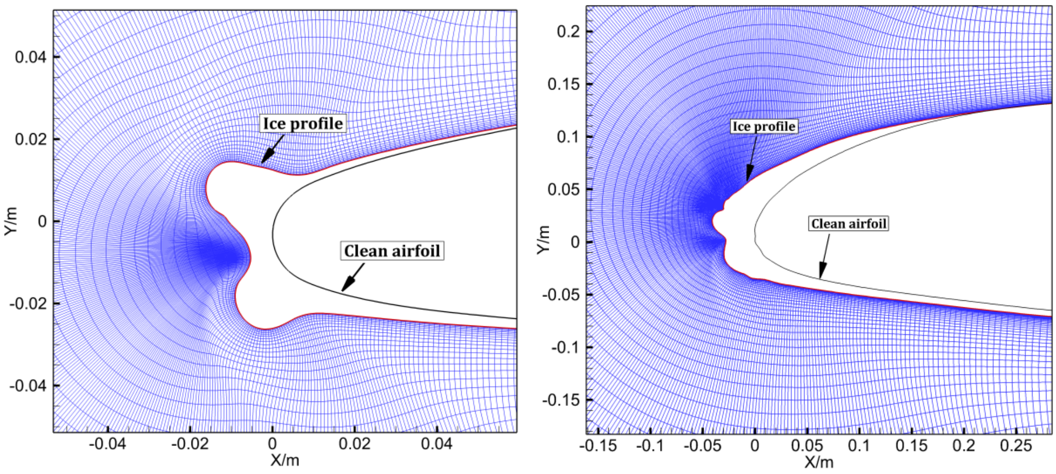

(a) GLC-305 (MVD=119μm) (b) NACA-23012 (MVD=225μm)

Fig.17 Meshes construction during ice accretion simulation

Fig. 18(a) and (b) present the predicted and experimental ice shapes on the airfoils of GLC-305 and NACA-23012 at MVD=119 μm and 225 μm. As can be observed, for both two cases, the predicted ice shapes obtained with the current splashing model (referred to "splashing case" for convenience) agree better with the experimental shapes compared to the calculated ice shapes without the splashing model (referred to "nonsplashing case" for convenience). The experiment demonstrated three typical ice horns , horn 1-3, as shown in Fig. 18(a), which is a typical glaze ice. Although both the predicted ice shapes are performed with two ice horns, the splashing cases are closer to the experimental results for horn 1 and horn 2 at thickness and angles. The experimental ice shape in Fig. 18(b) also shows typical ice horns which was observed at much lower temperature (rime icing condition). The ice shape in splashing case demonstrates four main ice horns, horn 1-4, at the leading edge while in the nonsplashing case only two ice horns, horn 1'-2', were captured. And the shapes of horn 1 and horn 2 are closer to the experimental ones compared to horn 1' and horn 2'. It is also noted that the ice shapes in the splashing case are thinner than that in the nonsplashing case. This is mainly due to the liquid mass loss caused by droplet splashing as mentioned in section 5.1.

In addition, the above comparisons also show the complexities of SLD icing: more and larger ice horns appear in both glaze and rime icing conditions. The splashing model can help in predicting droplet collection and re-impingement on other parts as described in Refs.[Tan & Papadakis, 2005; Wang et al., 2014], but it cannot be able to solve all the problems exist in SLD icing. Further researches on SLD icing mechanism are still required and this will be presented in our future work.

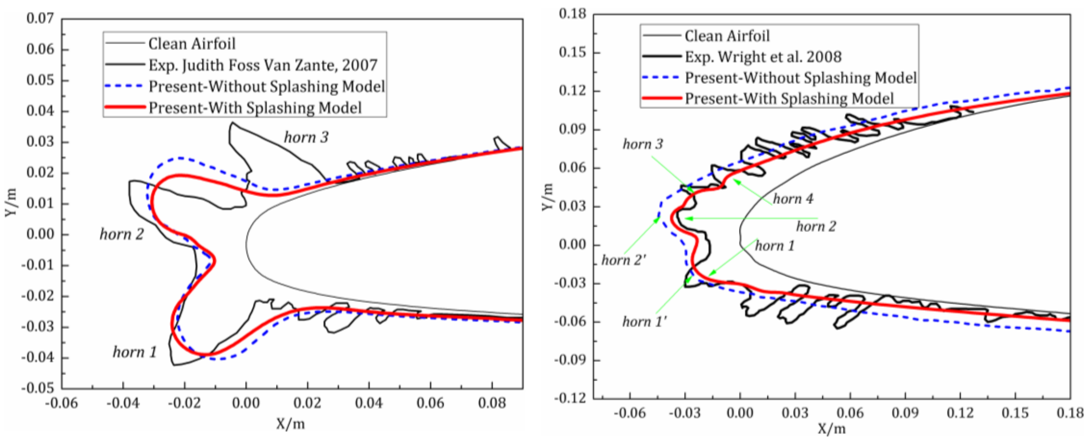

(a) GLC-305 (MVD=119μm) (b) NACA-23012 (MVD=225μm)

Fig.18 Comparison of the predicted ice shape and the experimental result

5.3 Droplet Impingement During Ice Accretion

In this section, changes of the mass fraction of the droplet splashing and reimpinging during ice accretion will be analyzed. The mass fraction of the droplet reimpinging (refer to “mass back ratio” for convenience) denotes the ratio of the quantity of the reimpinging mass to the total liquid mass collected by the control volume[Wang et al., 2014]. The test conditions are the same with that in section 5.2. Fig. 19(a) and (b) demonstrate the distribution of the mass loss ratio on surfaces with ice accretion. It is clearly seen that the droplet splashing mass loss performs gradually increasing tendency on the clean airfoil surface along chordwise direction. While with the increase of the ice accretion, this regular tendency was disturbed. This is due to the fact that the iced shape influences the flow field, then the droplet properties i.e. trajectory, impaction energy and angle, are thus changed. It is also noted that the mass loss ratio is zero on the back of the ice horn surface as shown in Fig.19(a) and this is due to no droplet impinging in this area.

Unlike the mass loss ratio, the distribution of the mass back ratio on surface is at a lower level, about 0~0.4, and in limited area as shown in Fig.20(a) and (b). It should be noted that the value of mass back ratio is almost zero on clean airfoil surface. And the mass back ratio is mainly distributed at the bottom area between two ice horns.

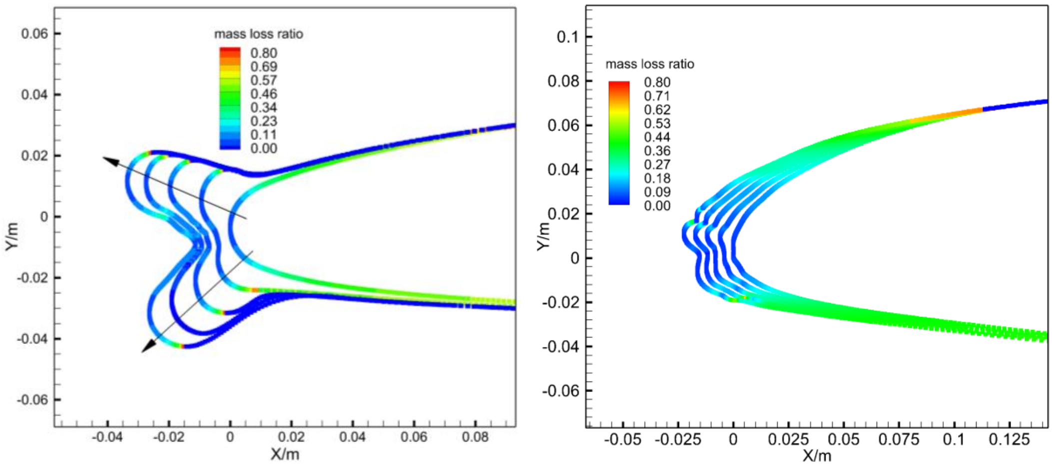

(a) GLC-305 (MVD=119μm) (b) NACA-23012 (MVD=225μm)

Fig.19 Distribution of the splashing mass loss ratio on airfoils' surfaces during the process of ice accretion

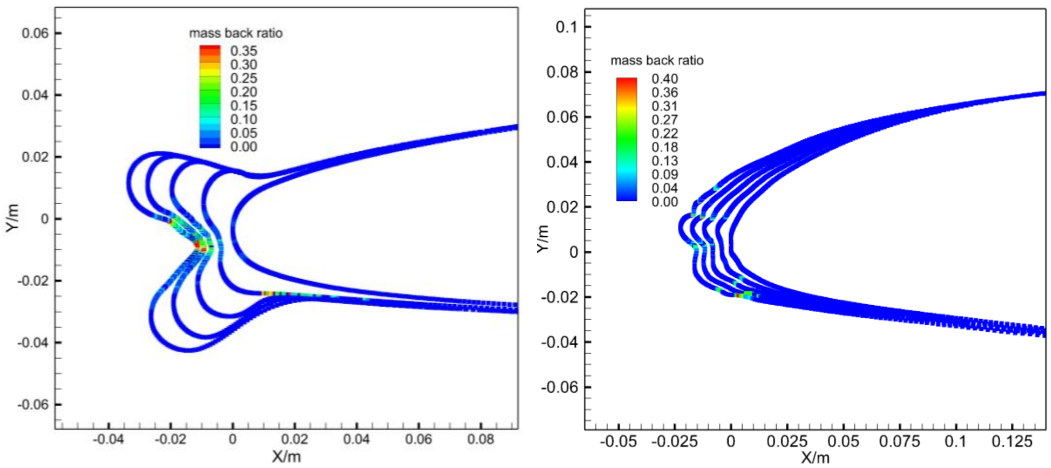

(c) GLC-305 (MVD=119μm) (d) NACA-23012 (MVD=225μm)

Fig.20 Distribution of the splashing mass back ratio on surfaces during the process of ice accretion

6. Conclusions

This article presented an overview of the physical phenomena associated with SLD impingement on surfaces, as well as a two-dimensional semiempirical splashing model to predict the SLD impingement on curved surfaces. Average values of the droplet impaction energy and angle were introduced in order to calculate the droplet impingement properties based on the micro-control volume in Lagrangian frame. In order to explore the effect of the droplet impaction energy and angle on droplet splashing, we defined the splashed mass loss ratio as the function of the available LEWICE numerical droplet collection efficiencies and experimental ones. It is worthy to note that the splashed mass loss ratio performs a decreasing tendency with the increase of droplet impaction energy and with the decrease of incident angle on curved surfaces. Therefore, the splashing criteria as well as the splashing mass loss ratio were suggested as the function of the droplet impaction energy and angle. Velocity of the splashed droplet was determined by solving an energy conservation equation. Considering the current computing capacity and the characteristics of 2D simulation, large number of the splashed smaller droplets generated in a real splashing case was simplified to one droplet. The model can be extended to three-dimensional as long as the sizes and amount of the splashed droplets are known.

The current splashing model was employed for the calculation of the droplet collection efficiency on different surfaces of the airfoil models, namely MS-317, NACA23012, GLC-305 and NACA65$_2$415, and SLD ice shapes on the airfoil models of GLC-305 and NACA23012 under glaze icing condition and rime icing condition, respectively. The current model provides a reasonably good prediction of the droplet collection efficiency particularly in the area close to the impinging limits.

In general, the ice shapes obtained by the current model show better agreement with the experimental ones compared to the ice shapes obtained in nonsplashing case.

Distributions of the droplet splashing mass loss ratio and reimpinging mass back ratio on surfaces during the process of ice accretion were calculated. Both two parameters were significantly influenced by surface shape at quantity and distribution characteristic. It should be noted that the interaction between the droplet splashing and reimpinging as well as ice accretion is mutual. Droplet splashing and reimpinging affects liquid water collection on surface, and then the amount and shape of the ice accretion were changed accordingly. In turn, the ice shape affects the profile of flow field, then the droplet properties, i.e. trajectory, impaction energy and angle, are thus influenced.

Acknowledgements

This work was financially supported by National Natural Science Foundation of China under Grant No. 11372026 and No. 11072019. The authors would like to thank Mrs. Lili Liu for her many contributions to this research.

References

[1] Alejandro Feo, Mario Vargas, Suthyvann Sor, 2011. Rotating Rig Development for Droplet Deformation/Breakup and Impact Induced by Aerodynamic Surfaces. SAE 2011-38-0087.

[2] C. Mundo, M. Sommerfield and C. Tropea., 2001. Droplet-Wall Collision: Experimental Studies of the Deformation and Breakup Process. **International Journal of Multiphase Flow** 11, 85-105.

[3] C. Mundo, M. Sommerfield, C. Tropea., 1995. Droplet-wall Collisions: Experimental Studies of The Deformation and Breakup Process. **International**

Journal of Multiphase Flow 21, 151-173.

[4] C. Bai, A.D. Gosman., 1995. Development of Methodology for Spray Impingement Simulation. SAE Paper, No.950283.

[5] C. Wang, S. Chang, H. Wu, 2014. Lagrangian Approach for Simulating Supercooled Large Droplets' Impingement Effect. **Journal of Aircraft** 52, 524-537.

[6] C. Wang, S. Chang, M. Wu, J. Jin., 2014. Numerical investigation of Splashing Characteristics in Super-cooled Large Droplet Regime. **Acta Aeronautica et Astronautica Sinica** 35, 1004-1011. (In Chinese)

[7] D. Kalantari, C. Tropea, 2007. Spray Impact onto Flat and Rigid Walls: Empirical Characterization and Modelling. **International Journal of Multiphase Flow**, 33(5): 525-544.

[8] G.E. Cossali, A. Coghe, M. Marengo, 1997. The Impact of a Single Drop on a Wetted Solid Surface. **Experiments in Fluids** 22, 463-472.

[9] G. Luxford, 2005. Experimental and Modeling Investigation of the Deformation, Drag and Break-Up of Drizzle Droplets Subjected to Strong Aerodynamic Forces in Relation to SLD Aircraft Icing. PhD. Thesis, Cranfield University, pp.103–113.

[10] Judith Foss Van Zante, 2007. A Database of Supercooled Large Droplet Ice Accretions. NASA/CR-2007-215020, SAE 2007-01-3348.

[11] M.F. Trujillo, W.S. Matthews, C.F. Lee, et al., 2000. Modeling and Experiment of Impingement and Atomization of a Liquid Spray on a Wall. **International Journal of Engine Research** 1, 87-105.

[12] M. Papadakis, K.E. Hung, G.T. Vu, H.W. Yeong, C. Bidwell, M. Breer, T.J. Bencic, 2002. Experimental Investigation Of Water Droplet Impingement On Airfoils, Finite Wings, and an S-Duct Engine Inlet, NASA TM-2002-211700.

[13] M. Papadakis, H.W. Yeong, K.E. Hung, C.S. Bidwell, 2004. Water Impingement Experiments on a NACA 23012 Airfoil with Simulated Glaze Ice Shapes. AIAA 2004-0565.

[14] M. Papadakis, S.C. Wong, A. Rachman, et al., 2007. Large and Small Droplet Impingement Data on Airfoils and Two Simulated Ice Shapes. NASA TM-2007-213959.

[15] M. Papadakis, A. Rachman, S.C. Wong, et al., 2007. Water Droplet Impingement on Simulated Glaze, Mixed, and Rime Ice Accretions. NASA TM-2007-213961.

[16] M.G. Potapczuk, 2003. Ice Mass Measurements: Implications for the Ice Accretion Process. AIAA 2003-387.

[17] M. John, 1996. A Forecast and Verification Experiment for Supercooled Large Drops (SLD). AIAA-96-0931.

[18] Philippe Villedieu, Pierre Trontin, Didier Guffond, David Bobo, 2012. SLD Lagrangian Modeling and Capability Assessment in the Frame of ONERA 3D Icing Suite, AIAA 2012-3132.

[19] P. Berthoumieu, 2012. Experimental Study of Supercooled Large Droplets Impact in an Icing Wind Tunnel. AIAA 2012-3130.

[20] R. Honsek, W.G. Habashi, M.S. Aubé, 2008. Eulerian Modeling of In-flight Icing due to Supercooled Large Droplets. **Journal of Aircraft** 45, 1290-1296.

[21] R.W. Gent, J.M. Ford, R.J. Moser, M.D. Miller, 2003. Results from Super-cooled Large Droplet Mass Loss Tests in the Act Luton Icing Wind Tunnel. AIAA 2003-389.

[22] R. Clift, J.R. Grace, M.E. Weber, 1978. Bubbles, Drops and Particles. **Academic Press**, New York, pp. 259–279.

[23] S.C. Tan, M. Papadakis, M.D. Miller, et al., 2007. Experimental Study of Large Droplet Splashing and Breakup. AIAA 2007-904.

[24] S.C., Tan, 2004. A Tentative Mass Loss Model for Simulating Water Droplet. AIAA 2004-0410.

[25] S.C., Tan, M. Papadakis, 2005. Droplet Breakup, Splashing and Re-Impingement on an Iced Airfoil. AIAA 2005-5185.

[26] W.B. Wright, M.G. Potapczuk, L.H. Levinson, 2008. Comparison of LEWICE and Glenn ICE in the SLD Regime. AIAA-2008-0439.

[27] W.B. Wright, 2006. Further Refinement of the LEWICE SLD Model. AIAA 2006-464.

[28] W.B. Wright, M.G. Potapczuk, 2004. Semi-Empirical Modeling of SLD Physics. AIAA 2004-412.

[29] Y. Li, C. Wang, S. Chang, D. Chen, 2011. Simulation of Ice Accretion Based on Roughness Distribution. **Procedia Engineering** 17, 160-177.

[30] Z. Han, Z. Xu, N. Trigui., 2000. Spray/wall Interaction Models for Multidimensional Engine Simulation, **International Journal of Engine Research** 1, 127-146.

Appendix: Results of Droplet Splashing Mass Loss

Appendix Table 1 Conditions for data preparation

Items	$MVD/\mu m$	$LWC/g.m^{-3}$	Λ
Case1	79	0.496	1.19×10^{-2}
Case2	94	0.22	0.91×10^{-2}
Case3	111	0.73	1.35×10^{-2}
Case4	137	0.68	1.32×10^{-2}
Case5	168	0.75	1.36×10^{-2}
Case6	236	1.89	1.85×10^{-2}

Appendix Table 2 Mass loss under different impaction energy and angles

	$\cos\bar{\theta}$	$\bar{K}_{m,up}$	$\bar{K}_{y,up}$	$\bar{f}_{up,exp}$	$\bar{K}_{m,dw}$	$\bar{K}_{y,dw}$	$\bar{f}_{dw,exp}$
Case1	1	589	128	0.17	589	128	0.17
Case1	0.9	526	121	0.23	516	120	0.22
Case1	0.8	450	112	0.26	455	112	0.22
Case1	0.7	390	104	0.28	384	103	0.16
Case1	0.6	334	96	0.23	308	92.5	0.13
Case1	0.5	260	85	0.19	243	82	0.25
Case1	0.4	182	71	0.24	165	68	0.44
Case1	0.3	109	55	0.44	145	63	0.65
Case1	0.2	84	48	0.54	96	52	0.8
Case1	0.1	38	32	0.71	36	32	0.92
Case1	0.05	19	23	0.78	17	22	0.96
Case2	1	700	154	0.18	700	154	0.18
Case2	0.9	626	146	0.17	618	145	0.15
Case2	0.8	534	135	0.17	537	135	0.17
Case2	0.7	478	127	0.15	452	124	0.16
Case2	0.6	396	116	0.13	375	113	0.23
Case2	0.5	320	104	0.17	296	100	0.38
Case2	0.4	233	89	0.18	213	85	0.22
Case2	0.3	123	65	0.47	179	78	0.49
Case2	0.2	89	55	0.66	97	57	0.78
Case2	0.1	48	40	0.81	43	38	0.96
Case2	0.05	23	28	0.9	18	25	1
Case3	1	768	139	0.11	768	139	0.11
Case3	0.9	653	128	0.19	690	132	0.18
Case3	0.8	574	120	0.21	598	123	0.23
Case3	0.7	539	117	0.23	507	113	0.25

Case3	0.6	398	100	0.28	410	102	0.22
Case3	0.5	336	90	0.21	336	92	0.33
Case3	0.4	252	80	0.5	248	79	0.24
Case3	0.3	175	66.5	0.68	167	65	0.43
Case3	0.2	102	51	0.82	102	51	0.56
Case3	0.1	40	32	0.9	28.6	26.9	0.83
Case3	0.05	12	17.4	0.98	11.3	17.1	0.95
Case4	1	993	160	0.16	993	160	0.16
Case4	0.9	897	152	0.14	879	150	0.17
Case4	0.8	765	140	0.17	758	139.5	0.18
Case4	0.7	648	128	0.24	643	128	0.14
Case4	0.6	543	118	0.21	540	118	0.16
Case4	0.5	452	108	0.17	423	104	0.22
Case4	0.4	321	90	0.16	311	89	0.33
Case4	0.3	243	79	0.35	270	83	0.54
Case4	0.2	95	49	0.56	140	60	0.66
Case4	0.1	58	39	0.75	58	39	0.81
Case4	0.05	25	25	0.9	21	23	0.82
Case5	1	1188	173	0.05	1188	173	0.05
Case5	0.9	1081	165	0.08	1044	162	0.14
Case5	0.8	916	152	0.14	919	152	0.10
Case5	0.7	773	139	0.11	773	139	0.10
Case5	0.6	628	126	0.10	640	127	0.11
Case5	0.5	520	114	0.09	508	113	0.15
Case5	0.4	404	101	0.09	366	96	0.31
Case5	0.3	305	88	0.22	327	91	0.42
Case5	0.2	102	51	0.42	162	64	0.77
Case5	0.1	41	32	0.65	70	42	0.75
Case5	0.05	29	27	0.88	25	25	0.8
Case6	1	1517	174	0.01	1517	174	0.01
Case6	0.9	1371	165	0.15	1400	167	0.01
Case6	0.8	1187	154	0.11	1169	153	0.02
Case6	0.7	1034	144	0.12	1037	144	0.05
Case6	0.6	782	125	0.16	807	127	0.2
Case6	0.5	620	116	0.2	620	111	0.27
Case6	0.4	459	96	0.36	480	98	0.18
Case6	0.3	321	80	0.52	339	82	0.22
Case6	0.2	175	59	0.8	187	61	0.29
Case6	0.1	70	37.4	0.95	43	29.3	0.92
Case6	0.05	25	22.3	1	9.2	20.45	1

Note: the subscripts “up” and “dw” denote upper surface and lower surface of the airfoil model, respectively.